Electronic Supplementary Information

Unveiling the atomistic mechanisms for oxygen intercalation in a strongly interacting graphene-metal interface

C. Romero-Muñiz[‡],[1] A. Martín-Recio[‡],[2] P. Pou,[1,3]

J. M. Gómez-Rodríguez,[2,3,4,][*] and Rubén Pérez[1,3,][†]

[1]*Departamento de Física Teórica de la Materia Condensada,*

Universidad Autónoma de Madrid, E-28049 Madrid, Spain[‡]

[2]*Departamento de Física de la Materia Condensada,*

Universidad Autónoma de Madrid, E-28049 Madrid, Spain

[3]*Condensed Matter Physics Center (IFIMAC),*

Universidad Autónoma de Madrid, E-28049 Madrid, Spain

[4]*Instituto Nicolás Cabrera (IFIMAC), Universidad*

Autónoma de Madrid, E-28049 Madrid, Spain

[*] josem.gomez@uam.es

[†] ruben.perez@uam.es

[‡] These authors contributed equally to this work.

CONTENTS

S1. FINAL STRUCTURE OF THE OXYGEN INTERCALATION ON G ON Rh: G/O−(2 × 1)/Rh(111)
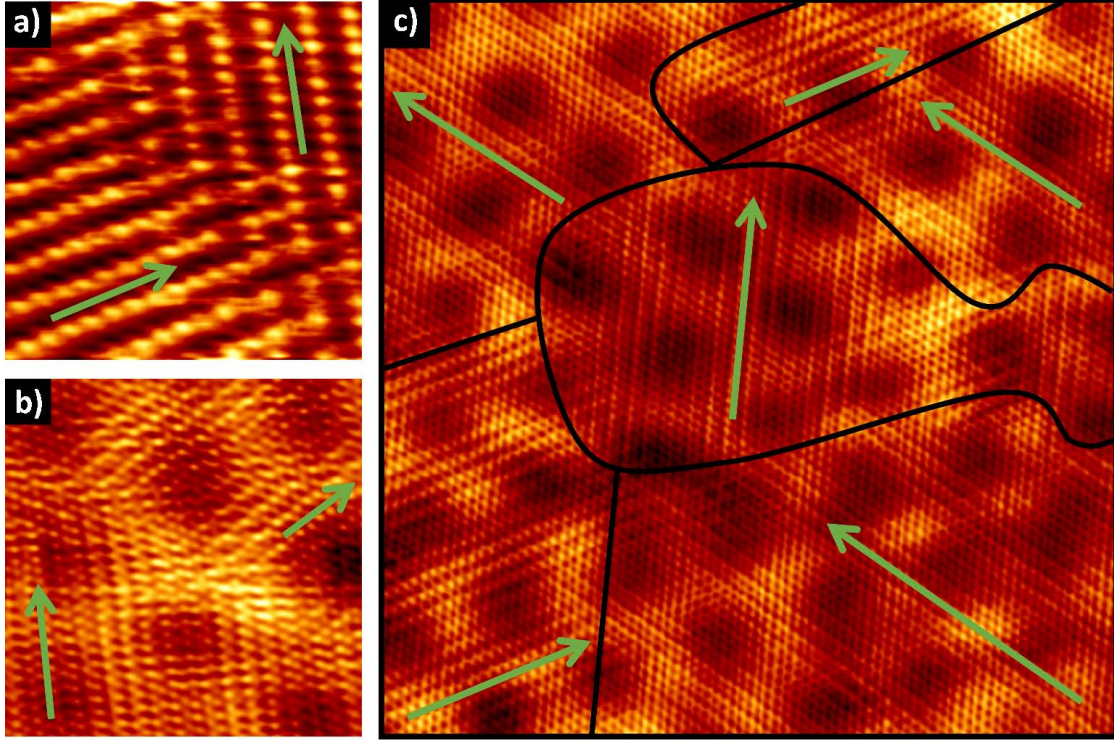

FIG. S1. Oxygen configuration on bare Rh(111) (a) and underneath graphene (b,c). (a) 3.6×3.6 nm^2 (160 mV, 4.6 nA). On clean Rh(111) the three domains of the 2×1 structure have been observed. The direction of the compact oxygen rows are indicated by green arrows. (b) 7×7 nm^2 (900 mV, 4.8 nA); (c) 17×17 nm^2 (600 mV, 6.6 nA). In both images, several oxygen rotational domains are observed through the graphene layer.

We have experimentally studied the oxygen intercalation as a function of the exposure time. For the larger exposure times used in the experiments, the oxygen atoms intercalate and diffuse until covering the whole interface [1]. Here we show our experimental results for this last intercalation stage.

Chemisorption of oxygen on transition metals has already been deeply studied finding mainly 2×2, 2×1 oxygen reconstructions if the temperature of the sample and/or the oxygen partial pressure during its preparation do not exceed certain values [2–5]. As an example of this, Fig. S1a is an STM image of O/Rh(111) without the graphene layer, where two different 2×1 oxygen rotational domains were observed. The presence of graphene could

change the arrangement of oxygen atoms on the metal surface. For example, Martínez-Galera *et al.* [6] showed the formation of two dense oxygen structures in the G/Ir(111) interface that do not exist without the graphene layer. However, we have found that at the G/Rh(111) interface, the oxygen atoms are adsorbed with respect to the metal surface in the 2×1 reconstruction. Both STM images and LEED measurements (see Fig. 1b in main text) only show this periodicity for the final stage of the intercalation. Figs. S1b and S1c are two areas of this surface in which different orientations of the 2×1 oxygen structure are observed. The direction of the compact oxygen rows are indicated by green arrows in the figure. No other structures have been observed with the preparation method used here. This does not discard the possibility of the formation of more compact structures if the oxygen pressure is further increased during sample preparation [6].

S2.   METHODS: DFT SIMULATIONS

Our theoretical approach in this study consists in performing density functional theory (DFT) calculations using the plane-wave basis code VASP [7] with a cutoff of 400 eV to ensure a proper energy convergence. Pseudopotentitals for all species were built using the PAW method [8, 9]. A Generalized Gradient Approximation was used for the exchange and correlation functional as described by Perdew, Burke and Ernzerhof (PBE-functional) [10] with the D2 semi-empirical correction [11] to take into account dispersion forces. In this kind of strongly-interacting systems, dispersion forces play a crucial role in the description of the interaction between the G and the metallic surface so they must be taken into account. Otherwise the obtained results, especially in corrugations, are erroneous [12, 13]. Spin polarization is not required in any of the calculations.

Initially we tested our computational machinery by characterizing the bulk Rh, the Rh(111) surface, the G and the O/Rh(111) system. We obtained: 3.7729 Å for the Rh bulk lattice parameter (which corresponds to 2.6678 Å for the Rh(111) lattice parameter) and 2.4678 Å for the G lattice parameter (1.4248 Å in the C–C distance). All these values are very close to their corresponding experimental ones (3.80 Å for bulk rhodium [14] and 1.42 Å for the C–C distance in G [15]). We also were able to reproduce previous theoretical calculations on the O–(2×1)/Rh(111) and O–(2×2)/Rh(111) systems [16] both in structural parameters (i.e. O–Rh bond length of 2.00 Å) and adsorption energies (see table S1), in very good agreement with experimental results [4].

Periodic boundary conditions are used in the simulations with different unit cells. Due to the system size, most of the calculations are performed on a unit cell constituted by a $[(\sqrt{43} \times \sqrt{43})$-R7.6°$]_\mathrm{G}$ on a $(6 \times 6)_\mathrm{Rh}$. This rhombic unit cell has a side of 16.17 Å and contains 230 atoms (excluding oxygen atoms). However we have also used other larger cells; $[(\sqrt{91} \times \sqrt{91})$-R27°$]_\mathrm{G}$ on $[(2\sqrt{19} \times 2\sqrt{19})$-R23.4°$]_\mathrm{Rh}$ and $(12 \times 12)_\mathrm{G}$ on $(11 \times 11)_\mathrm{Rh}$. They contain 486 and 772 total atoms and their sizes are 23.50 Å and 29.66 Å respectively. All systems used in simulations have been observed and fully characterized by STM experiments in our previous work [17]. In all cases the unit cell results from the superposition of a four-layer rhodium slab and the G monolayer plus a variable number of oxygen atoms, leaving more than 14 Å of vertical spacing between periodical images along the z axis. The procedure to build this kind of cells avoiding the mismatch between the two lattices is not trivial and

	Binding (Adsorption) Energy (eV/O atom)			
	fcc adsorption		hcp adsorption	
work and functional	2×1	2×2	2×1	2×2
ref. [16] (PBE)	$-4.93(-1.95)$	$-5.22(-2.24)$	$-4.79(-1.81)$	$-5.11(-2.13)$
Our work (PBE)	$-4.90(-1.87)$	$-5.18(-2.15)$	$-4.73(-1.70)$	$-5.07(-2.04)$
Our work (PBE-D2)	$-5.01(-1.98)$	$-5.26(-2.23)$	$-4.85(-1.82)$	$-5.17(-2.14)$

TABLE S1. Comparison of adsorption energies for atomic oxygen on Rh(111) both in (2×2) and (2×1) cells considering adsorption on fcc-hollow and hcp-hollow sites. Notice how dispersion forces do not affect significantly due to the chemisorbed nature of the adsorption.

it is explained in detail in our previous work [17]. These structures were subjected to ionic relaxations following a conjugate gradient algorithm until forces upon atoms were less than 0.01 eV/Å. During these relaxations, the two deepest layers of the slab were kept fixed in their bulk positions while all the rest, including oxygen atoms, were allowed to relax. The reciprocal space was sampled using a $2 \times 2 \times 1$ Monkhorst-Pack grid [18], except in the largest unit cell where only the Γ point was used.

Finally, the climbing image Nudged Elastic Band (CI–NEB) method [19] was used to determine the energy barriers in the diffusion processes of atomic oxygen, using five intermediate images in each calculation. In this case the convergence criterion in forces was lowered to 0.05 eV/Å and the spring constant between images was set to 1.5 eV/Å^2.
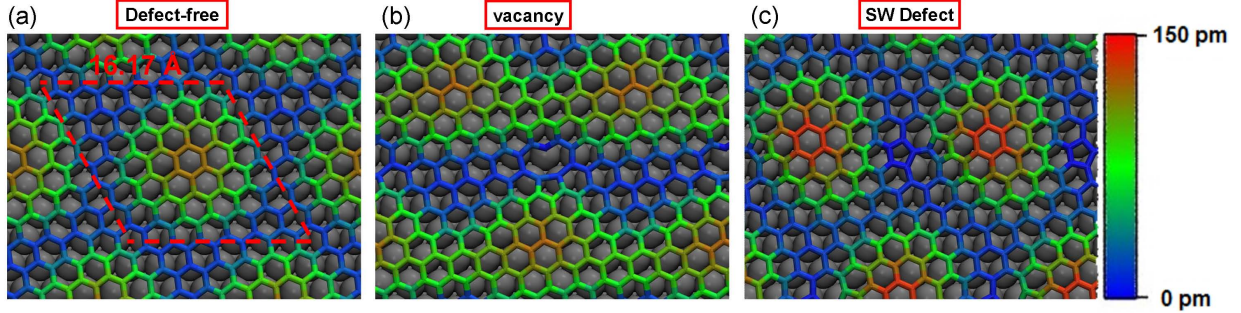
S3. OXYGEN PENETRATION THROUGH POINT DEFECTS ON G/Rh(111)

FIG. S2. Top views of the G/Rh(111) system in the $[(\sqrt{43} \times \sqrt{43})\text{-R7.6°}]_G$ unit cell. Defect-free (a), monovancacy (b) and Stone-Wales defect (c). Notice how the two different point defects tend to approach to the surface due to its high reactivity.

We have investigated, using DFT simulations, the possibility of an atomic oxygen to pass through point defects on the graphene layer. We have focused our study on two of the most common, and representative, point defects: a monovancay, that is characterized by the presence of a carbon atom with a dangling bond [20] and a Stone-Wales defect, with the typical 7-5 ring structure [21], that also appears in other defects as grain boundaries. Our results show that oxygen penetration through them is not possible.

We first show how these defects behave on the G/Rh(111) system. In Fig. S2 we show the relaxed structures of the most stable configuration of both systems in comparison with the structure of the defect-free moiré pattern. Although atomic arrangements are similar to those in the free standing cases (we still observe the 5-9 asymmetric reconstruction of the monovacancy [20] and the 5-7 structure of the SW), we found relevant differences: (1) Both defects tend to downward the layer towards the metal due to the strong defect-metal interaction. For example, the energy of creating a monovacancy in the high part of the moiré is 2.1 eV larger than the creation energy of a vacancy in the lower parts. (2) In the monovancancies, similarly to that found in G/Pt(111) [22], the carbon atom with the dangling bond moves ~ 1 Å and binds strongly to the metal, even when the vacancy is in the high part of the moiré. (3) The defect-metal hybridization broad and shift the electronic states associated with the defects, quenching any magnetic properties that these point defects could present in the free standing case [23].

Next, we analyze the possibility of oxygen penetration through the monovacancies. In

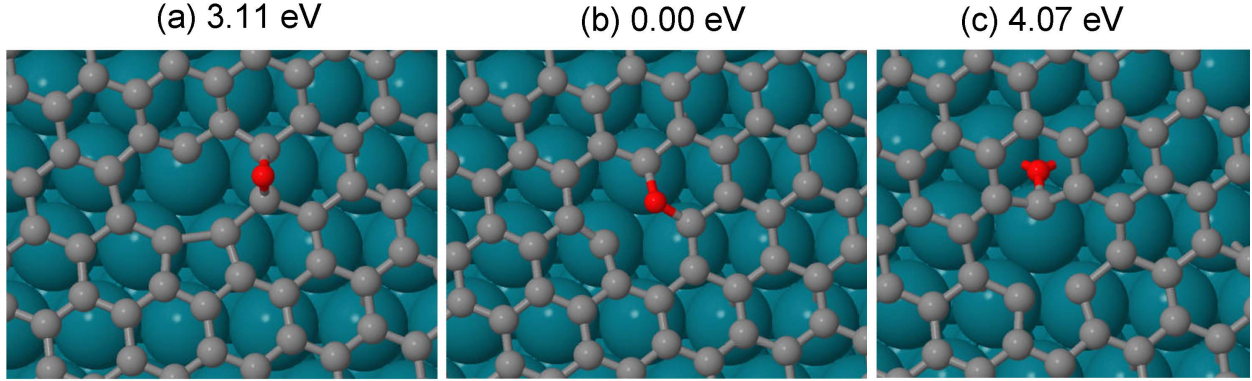(a) 3.11 eV   (b) 0.00 eV   (c) 4.07 eV

FIG. S3. Different equilibrium structures of an oxygen atom in the neighborhood of a vacancy in the graphene layer in the G/Rh(111) system. (a) Adsorbed on near bridge position, (b) just in the vacancy, and (c) under the graphene layer. In each case it is displayed the relative energy of the structure showing that the vacancy-oxygen atom pair forms a very stable configuration much more energetically favourable than any other possible adsorption configuration, making the penetration energy barrier very high.

the free-standing case we find that the oxygen atom tends to place just inside the vacancy and saturate the dangling bonds of the carbon atoms, i.e. it substitutes the missing carbon. This configuration is 5.4 eV more stable than that of the following stable configuration characterized by the oxygen adsorbed on a bridge position close to the vacancy. This result could be expected as the creation of a monovacancy requires ~ 8 eV [23]. The high stability of the oxygen inside the vacancy prevents, in free standing graphene, any oxygen penetration through monovacancies. The presence of the metal surface, although it induces relevant differences, keeps the basic idea: the oxygen inside the defect is the most stable configuration. The energy difference is now reduced. We can estimate it to be ≥ 3 eV, as this is the energy difference, for the most extreme case of a monovacancy in the lowest moiré parts, between the most stable configuration and one with the vacancy and an oxygen atom already in the most favorable site in the G-metal interface (see Fig. S3). We should notice that in the G/Rh(111) case, the most stable configuration differs from the free-standing case, the oxygen atom just bonds with two carbon atoms as the third carbon is bonded to the metal. Moreover, it is important to highlight that our results completely differ from previous studies carried out for Si as the guest atom [24] in which they suggested very low energy values for the barriers (0.33 eV) of Si penetration through monovacancies in G/Ru(0001). These discrepancies
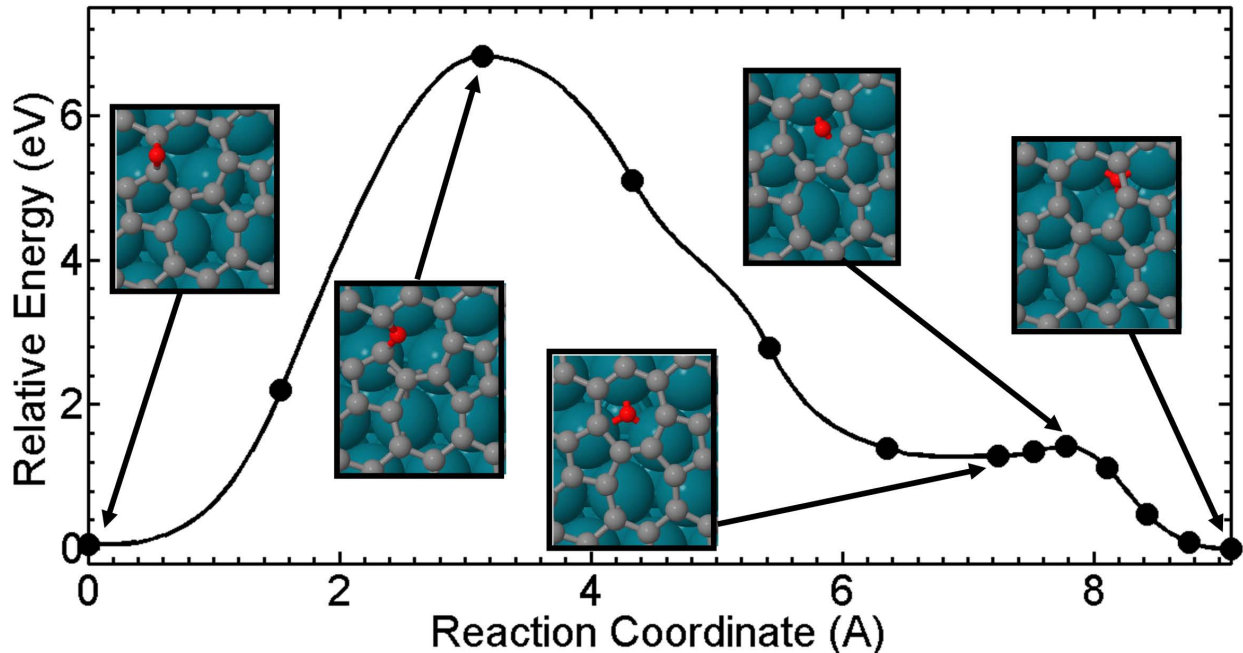
FIG. S4. Diffusion path of an oxygen atom penetrating through a SW defect in the G/Rh(111) surface. Notice how the hollow position just under the defect it is not very stable compared with an inner site. The penetration is carried out by breaking one of the C–C bonds in the heptagon of the SW defect.

arise from the fact that they do not consider the complete intercalation process in their calculations. Additionally, they did not consider the energy needed to extract the guest atom from the vacancy to the metal substrate and also they used a very simplified model for the simulation cell.

Regarding the SW defect, the absence of dangling bonds makes possible some stable structures with an oxygen atom adsorbed in one bridge position (see Fig. S4). In the G/Rh(111) system our DFT calculations show that the adsorption of an oxygen atom above the graphene layer near a SW defect is slightly less favorable than the intercalated config-uration in the same conditions with a minimal difference in energies of 0.06 eV. However, the energy barrier for the penetration, calculated using the CI–NEB method, is of 6.82 eV, preventing the possibility of oxygen penetration through one of the heptagons of the SW defects. This very high energy barrier is related with the requirement of breaking a C–C bond in the penetration path (see the transition state at Fig. S4).

These simulations show that penetration through purely point defects in this system is

very improbable. In fact, monovacancies would behave as attraction centers for oxygen atoms, trapping them inside the vacancy. On the other hand, SW defects will not be penetration ways as there is not room for an oxygen atom in the 7-ring and, consequently, penetration requires the breaking of a C–C bond.
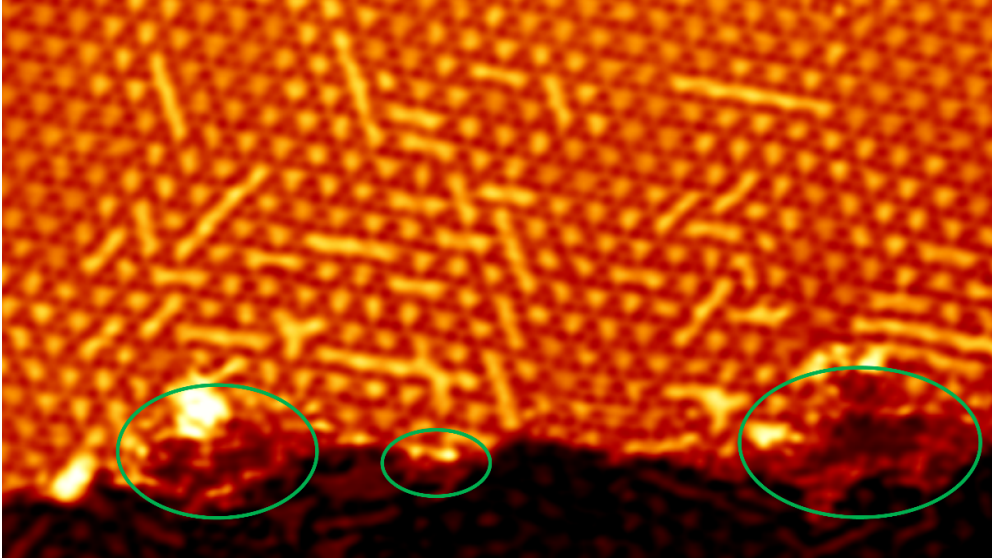
S4. GRAPHENE ETCHING AT THE STEP EDGES

FIG. S5. Graphene etching by oxygen atoms at 550 K. Some small graphene-free areas (marked with a green oval) are observed in this (80×45) nm^2 STM image (120 mV, 6.5 nA) measured at RT near the step edges where defect density is larger.

Small graphene etched areas were often found near surface step edges after oxygen exposure at 550 K. Before oxygen exposure, these graphene-free areas were never observed. Therefore we suggest they are due to oxygen etching of the graphene layer always at these step edges areas where the 2D layer has a larger defect density.

This effect can be observed in three different areas of the same surface step of Fig. 6 from the main article. The same surface area is shown here again as Fig. S5 in which the graphene etched areas have been highlighted with green ovals.

S5. OXYGEN DIFFUSION BARRIERS AT THE G/Rh(111) INTERFACE IN LARGE MOIRÉ CELLS.

In the main text we prove that atomic oxygen diffusion under the graphene is possible under the higher parts of the moiré cell. In these calculations we have used the cited $(6 \times 6)_{Rh}$ cell which shares the main features of the larger $(11 \times 11)_{Rh}$ moiré (i.e. similar corrugation, adsorption distances, etc.). However, in the largest moiré pattern (shown in Fig. 4c of the main text), which is also the most common, the highest moiré areas (red according to our color scale) are linked through mid-height regions (green). The reasons of using the small $(6 \times 6)_{Rh}$ cell for most of the simulations here presented instead the most common one, are obviously related to the highly-demanded computational requirements of performing calculations on large unit cells. Nevertheless, a few calculations in larger unit cells are required in order to disclose whether: (i) the energetic of the oxygen at the interface is mainly related with the G-metal separation; and (ii), as discussed in the main text, the oxygen diffusion between the highest parts of the moiré is possible through the mid-height regions that do not exist in the smaller moiré pattern.

We have calculated both the adsorption energies and the diffusion barrier in one of these mid-height regions in a cell with a $[(2\sqrt{19} \times 2\sqrt{19})\text{-R23.4°}]_{Rh}$ reconstruction on Rh(111) by highest parts are connected (see Fig. 4b in the main text). In this case, it is not affordable to use the CI–NEB formalism but it is possible to converge separately each frame of the path by imposing some boundary conditions. We fixed the xy positions of the atoms belonging to the G layer. This procedure is completely justified because the diffusion path is known with enough accuracy. In any case, this calculation yields an upper bound of the barrier height. In Fig. 4 of the main text, the calculated diffusion barrier is shown and its value is 0.71 eV. The adsorption energy at this zone of the moiré is increased by 0.69 eV (this is $E_1 - E_0$ in Fig. 4) respect to the oxygen intercalation in the highest parts. For the largest moiré pattern $(11 \times 11)_{Rh}$ this difference is even lower, 0.58 eV. Both the relative adsorption energy and diffusion barrier are very similar to those obtained in the smaller moiré cell in areas with similar G-metal separations. This result points out that the energetic of the oxygen in the G/Rh(111) interface depends mainly on this relative distance between the G layer and the metallic surface.

[1] C. Romero-Muñiz, A. Martín-Recio, P. Pou, J. M. Gómez-Rodríguez, and R. Pérez, Carbon **101**, 129 (2016).

[2] J. Gustafson, A. Mikkelsen, M. Borg, E. Lundgren, L. Köhler, G. Kresse, M. Schmid, P. Varga, J. Yuhara, X. Torrelles, C. Quirós, and J. N. Andersen, Phys. Rev. Lett. **92**, 126102 (2004).

[3] H. Over, Prog. Surf. Sci. **58**, 249 (1998).

[4] S. Schwegmann, H. Over, V. D. Renzi, and G. Ertl, Surf. Sci. **375**, 91 (1997).

[5] L. Köhler, G. Kresse, M. Schmid, E. Lundgren, J. Gustafson, A. Mikkelsen, M. Borg, J. Yuhara, J. N. Andersen, M. Marsman, and P. Varga, Phys. Rev. Lett. **93**, 266103 (2004).

[6] A. J. Marínez-Galera, U. A. Schroder, F. Huttmann, W. Jolie, F. Craes, C. Busse, V. Caciuc, N. Atodiresei, S. Blugel, and T. Michely, Nanoscale **8**, 1932 (2016).

[7] G. Kresse and J. Furthmüller, Phys. Rev. B **54**, 11169 (1996).

[8] G. Kresse and D. Joubert, Phys. Rev. B **59**, 1758 (1999).

[9] P. E. Blöchl, Phys. Rev. B **50**, 17953 (1994).

[10] J. P. Perdew, K. Burke, and M. Ernzerhof, Phys. Rev. Lett. **77**, 3865 (1996).

[11] S. Grimme, J. Comput. Chem. **27**, 1787 (2006).

[12] B. Wang, M. Caffio, C. Bromley, H. Früchtl, and R. Schaub, ACS Nano **4**, 5773 (2010).

[13] D. Stradi, S. Barja, C. Díaz, M. Garnica, B. Borca, J. J. Hinarejos, D. Sánchez-Portal, M. Alcamí, A. Arnau, A. L. Vázquez de Parga, R. Miranda, and F. Martín, Phys. Rev. Lett. **106**, 186102 (2011).

[14] J. W. Arblaster, Platin. Met. Rev. **41**, 184 (1997).

[15] A. H. Castro Neto, F. Guinea, N. M. R. Peres, K. S. Novoselov, and A. K. Geim, Rev. Mod. Phys. **81**, 109 (2009).

[16] M. V. Ganduglia-Pirovano and M. Scheffler, Phys. Rev. B **59**, 15533 (1999).

[17] A. Martín-Recio, C. Romero-Muñiz, A. J. Martinez-Galera, P. Pou, R. Pérez, and J. M. Gómez-Rodríguez, Nanoscale **7**, 11300 (2015).

[18] H. J. Monkhorst and J. D. Pack, Phys. Rev. B **13**, 5188 (1976).

[19] G. Henkelman, B. P. Uberuaga, and H. Jónsson, J. Chem. Phys. **113**, 9901 (2000).

[20] S. T. Skowron, I. V. Lebedeva, A. M. Popov, and E. Bichoutskaia, Chem. Soc. Rev. **44**, 3143 (2015).

[21] A. Stone and D. Wales, Chem. Phys. Lett. **128**, 501 (1986).

[22] M. M. Ugeda, D. Fernández-Torre, I. Brihuega, P. Pou, A. J. Martínez-Galera, R. Pérez, and J. M. Gómez-Rodríguez, Phys. Rev. Lett. **107**, 116803 (2011).

[23] L. Rodrigo, P. Pou, and R. Pérez, Carbon **103**, 200 (2016).

[24] G. Li, H. Zhou, L. Pan, Y. Zhang, L. Huang, W. Xu, S. Du, M. Ouyang, A. C. Ferrari, and H.-J. Gao, J. Am. Chem. Soc. **137**, 7099 (2015).